Nonlocal Phase-Coherent Coupling Between Rough-Wall Geometry and Space-Charge Modes in Plasma Sheaths

Chang Lu[1,*] and Pei Qiu[2]

[1] *State Key Laboratory of Industrial Equipment Structural Analysis and Optimization and CAE Software, Dalian University of Technology, Dalian, 116024, China*

[2] *College of Zhan Tianyou, Dalian Jiaotong University, Dalian, 116028, China*

The spatial low-pass character of vacuum electrostatic fields suggests that short-scale wall corrugations should leave only a weak direct signature at a distant inlet, motivating the wall-height power spectral density (PSD) as a predictor of upstream signatures. Here we reveal that this PSD-based prediction breaks down in a nonlinear plasma sheath: even in the simplest case of cold-ion Debye sheaths over rough walls with identical height PSDs, changing only the relative spatial phase of a shallow long-wavelength undulation markedly alters the maximum inlet field modulation. For the walls studied here with relief and peak spacing comparable to the sheath thickness, this phase sensitivity can surpass a factor of three. By decomposing the potential into vacuum and space-charge contributions, we show that short-wavelength corrugations deflect the near-wall ion flow and nonlinearly excite a long-wavelength space-charge mode. This self-generated field survives spatial filtering to the upstream inlet, where it coherently reinforces or cancels the response to the long wall undulation. Sweeping the relative spatial phase continuously tunes the sheath between coherent amplification and shielding at fixed roughness power, and this phase contrast persists across variations in wall bias, inlet Mach number, inlet height, and short-wave tuning. Because the inlet field modulation directly determines whether the external plasma can treat the rough wall as an equivalent plane, these results establish cross-scale spatial phase as a key control parameter linking microscopic wall geometry to the macroscopic plasma response.

Classical sheath theory assumes a one-dimensional planar wall [1], as in the space-charge laws [2, 3], whereas real plasma-facing surfaces in fusion divertors, semiconductor etching, and spacecraft charging exhibit complex, rough geometries [4–6]. Even so, representing a rough surface by an effective plane (hereafter exterior planar equivalence) remains highly desirable for simplifying both analysis and macroscopic modeling [7, 8]. Such planar equivalence holds for small-amplitude ripples and, locally, for gently curved surfaces via the tangent-plane approximation [9], but is generally expected to break down in the intermediate regime where roughness scales approach the sheath thickness. Yet in the linear half-space vacuum limit, an electrostatic perturbation of wave number k decays exponentially as $\exp(-|k|d)$ over distance d [10], acting as a low-pass filter through which only long-wavelength components propagate to the far field. Intuitively, therefore, if an intermediate-scale rough wall is dominated by short-wavelength features—with sheath-scale short-wave amplitudes far exceeding any long-wavelength undulation—its nonlocal influence on the exterior plasma should still be reducible to an effective planar sheath.

Yet direct sheath calculations reveal a striking breakdown of this intuition. As shown in Figure 1, two corrugated walls with nearly identical profiles—differing by less than 2% in maximum height deviation and sharing the exact same height power spectral density (PSD)—produce vastly different upstream responses: the transverse modulation at the inlet is below 4.5% (4.50%) in one case, yet exceeds 14% (14.21%) in the other. This paradox stems from nonlinear cross-scale coupling within the sheath: near-wall ion deflection [4, 11] and equipotential distortion by short-wavelength roughness [12] excite a long-wavelength space-charge field that reaches the upstream inlet, where the response to the weak long-wavelength wall undulation can either reinforce or cancel it. The natural questions are how this coherent interference arises, whether it can be tuned continuously and robustly at fixed roughness power, and what it implies for exterior planar equivalence.

Here, using cold-ion Debye sheaths over isospectral rough walls as an example, we demonstrate that neither the roughness amplitude nor the height PSD alone determines the upstream plasma response. Using a continuous family of isospectral walls, we isolate the cross-scale excitation of long-wavelength space charge, verify a predictive interference law across a full phase sweep, and show that the resulting phase sensitivity persists across plasma parameters and directly governs exterior planar equivalence. Building on these observations, we also derive a tolerance-based criterion for exterior planar equivalence.

Rough-wall sheath model and isospectral walls—We consider a steady, electrostatic, collisionless, and unmagnetized two-dimensional plasma sheath bounded by a periodic absorbing wall $z = h(x)$ of period L and a planar equipotential inlet at $z = H$. We measure length in reservoir Debye lengths λ_D, potential in T_e/e, density in units of the reservoir density, and velocity in the ion acoustic speed $c_s = \sqrt{T_e/m_i}$. For regular single-stream cold-ion

* Corresponding author: changlu@dlut.edu.cn

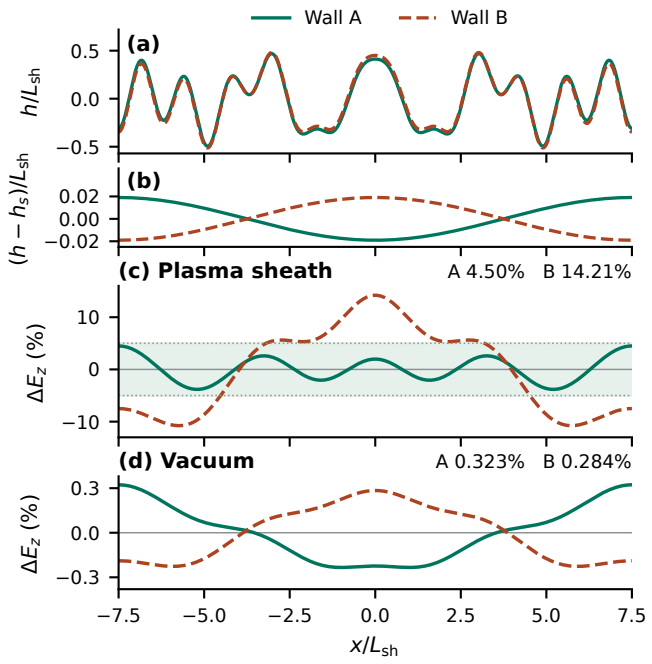


Figure 1. Isospectral walls viewed from the same upstream inlet. (a) Wall A ($\theta = \pi$) and wall B ($\theta = 0$). (b) Long corrugations after subtracting the shared short profile. Inlet normal-field variation $\Delta E_z = 100(E_z/\bar{E}_z - 1)\%$ in (c) the plasma sheath and (d) vacuum (expanded scale). Each trace uses its own mean. Labels give $\max|\Delta E_z|$. Shading marks $\pm 5\%$.

flow from the inlet toward the wall, the ion density n_i, velocity $\boldsymbol{u}$, and potential ϕ obey the fluid–Poisson system [13]

$$\nabla^2\phi = F_e(\phi) - n_i, \qquad n_e = F_e(\phi),$$
$$\nabla\cdot(n_i\boldsymbol{u}) = 0, \qquad (\boldsymbol{u}\cdot\nabla)\boldsymbol{u} = -\nabla\phi. \tag{1}$$

Here $F_e(p) = \frac{1}{2}\exp(p)[1 + \operatorname{erf}\sqrt{p - V}]$ is the prescribed local absorbing-electron response [14]. The nonemitting wall is held at $V < 0$. At the inlet, $\phi = 0$, $n_i = n_0 = F_e(0)$, and cold ions enter normally with $\boldsymbol{u} = (0, -M)$. The benchmark uses $V = -5$, $M = 1.2$, $H = 32$, and $L = 15L_{\rm sh}$, where $L_{\rm sh} = 6.894$ is the planar sheath thickness at the same bias and supply.

To isolate cross-scale phase coupling at fixed roughness power, we construct a continuous family of isospectral walls,

$$h_\theta(x) = h_s(x) + b\cos(k_1 x + \theta), \qquad k_n = 2\pi n/L. \tag{2}$$

The short-wavelength profile $h_s(x) = L_{\rm sh}\sum_n c_n\cos(k_n x)$ contains only modes $n = 4, 5, 11, 12$, with peak-to-valley height $0.98L_{\rm sh}$, and the coefficients c_n are approximately 0.22, 0.22, 0.16, and -0.17, while the long-wavelength profile has amplitude $b = 0.019L_{\rm sh}$. Because the two terms occupy disjoint Fourier bands, every member of the family shares the exact same height PSD. In this benchmark, the long-wavelength component of the vacuum inlet normal field produced by h_s alone is negligible.

Figure 1 compares wall A ($\theta = \pi$) with wall B ($\theta = 0$). Although their geometric profiles are nearly indistinguishable—and even in the full rough-domain vacuum calculation their relative inlet modulations are only 0.323% and 0.284%—their plasma responses diverge sharply. Defining the maximum relative inlet-field variation over the patch D (here one full period) as $\delta_D(H) = \max_{x\in D}|E_z(x,H) - \bar{E}_z(H)|/|\bar{E}_z(H)|$, where overbars denote transverse averages across D, we find that the two inlet means differ by only 0.53%, yet wall B's modulation (14.21%) is 3.16 times that of wall A (4.50%).

Cross-scale excitation and coherent interference—To identify the physical origin of the upstream modulation, we decompose the potential into a geometric vacuum part $\phi_{\rm vac}$, which solves Laplace's equation in the same rough domain with the same boundary potentials, and a space-charge part $\phi_{\rm sc} = \phi - \phi_{\rm vac}$. The latter is driven by the net charge density $\rho = n_i - n_e$ with homogeneous potential conditions on both the wall and the inlet. Below, we track the fundamental Fourier mode of the normal potential slope $a = -E_z$, whose amplitude and relative modulation are invariant under this sign convention.

With this decomposition in place, we can follow a wavelength from its appearance in the near-wall charge to its signature at the inlet. Short corrugations deflect and focus the incoming ions [11, 15]. Density and velocity variations multiply in the ion flux $n_i\boldsymbol{u}$, and the electron density responds nonlinearly to the potential. Both processes mix wave numbers: modes 4 and 5, for instance, can generate a difference mode $n = 1$ that varies once across the entire wall period. Modes 11 and 12 can contribute at the same wavelength. The short profile h_s shared by walls A and B contains only these four short modes [Figure 2(a)]. Yet just above the peaks, its net charge already has a long-wave component, visible beneath the sharper local variations in Figure 2(b).

Spatial filtering gives this long wave a larger share of the field variation farther upstream. Across a source-free strip of depth d, the transfer factor $-|k|/\sinh(|k|d)$ from a boundary potential harmonic to the normal potential slope at the opposite, equipotential boundary attenuates shorter wavelengths more strongly. In the sheath calculation, modes $n \geq 4$ account for 98.9% of the transverse field variance just above the peaks [Figure 2(c)]. At the inlet, the broad crest and trough follow mode 1, which alone accounts for 76.2% [Figure 2(d)]. For h_s alone, vacuum and space charge contribute $+0.025\%$ and -5.554% of the short-wall mean inlet slope $\bar{a}_{H,s}$ to the signed mode-1 coefficient. Thus nearly the entire inlet long wave comes from space charge.

Adding a shallow long wall corrugation changes both the geometric field and the space charge. Let S be the complex inlet coefficient of mode 1 for the short wall alone

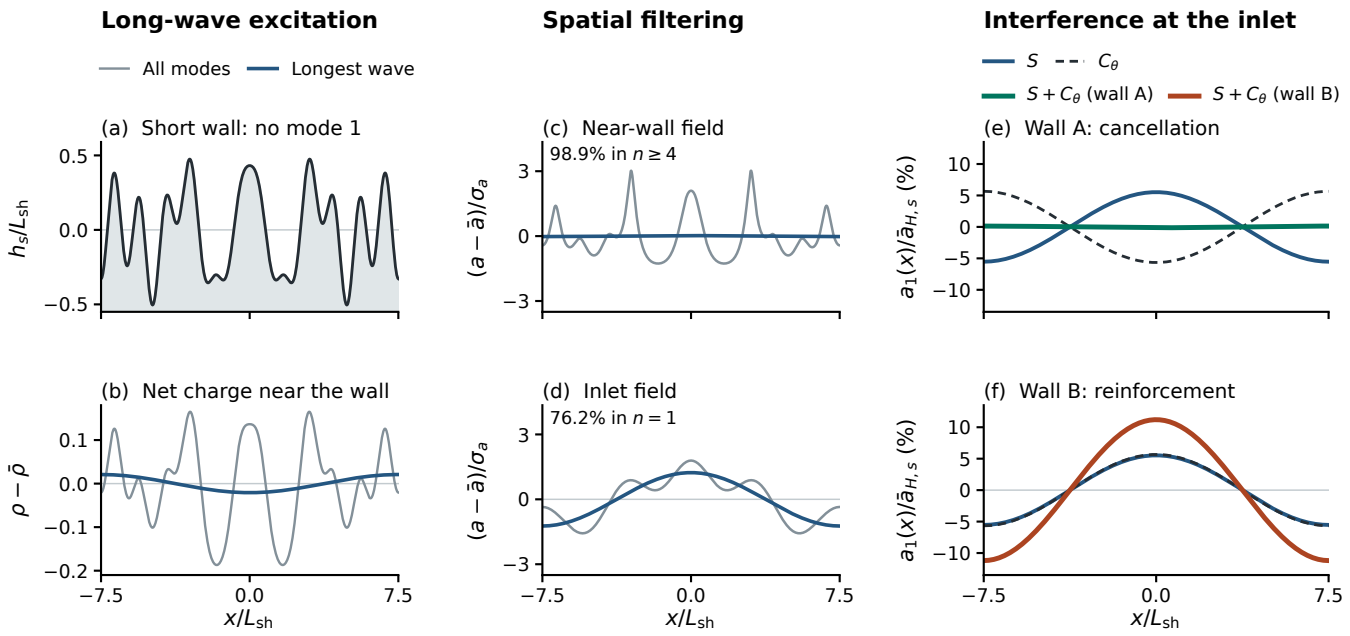


Figure 2. Long-wave excitation, spatial filtering, and interference. (a) Short wall h_s shared by A and B. (b) Net charge variation $0.1L_{\rm sh}$ above its highest peak. In (b–d), gray is the full variation and blue its longest wave ($n = 1$). (c,d) Normal field $a = -E_z$ at the same near-wall section and at the inlet, each centered on its own mean and scaled by its own standard deviation σ_a. Percentages give shares of the lateral field variance. (e,f) Inlet normal-field profiles reconstructed from the $n = 1$ Fourier coefficients. S (blue) is the complex coefficient for the short wall corrugations alone. C_θ (black dashed) is the coefficient for the combined wall at phase θ minus S. The green and orange curves show $S + C_\theta$ for walls A and B, respectively. All four curves are expressed as percentages of the short-wall inlet mean $\bar{a}_{H,s} = 2.81 \times 10^{-7}$.

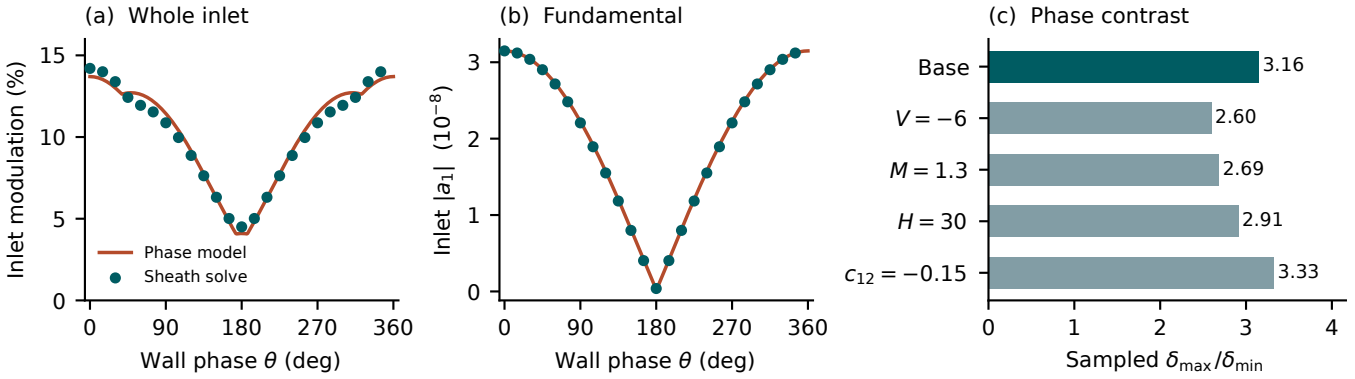


Figure 3. Phase control at fixed height PSD. (a) Maximum relative modulation of the entire inlet field. (b) Amplitude of its fundamental. Symbols are nonlinear sheath solutions. Curves use the short-wall field and only the $\theta = 0$ combined-wall result to predict the phase dependence. (c) Ratio of the largest to smallest sampled inlet modulation. Each row changes one parameter with all other inputs fixed. The baseline uses 15° phase steps and the four variations use 30° steps.

and C_θ the net change when the shallow long wall corrugation is added with spatial phase θ. The phase difference between S and C_θ is $\psi = \arg C_\theta - \arg S$, which determines the amplitude of the resulting long wave through

$$|S + C_\theta|^2 = |S|^2 + |C_\theta|^2 + 2|S||C_\theta| \cos\psi. \qquad (3)$$

S (blue line in Figure 2(e,f)) has amplitude 5.53% of $\bar{a}_{H,s}$. On wall A the crest of S meets the trough of C_θ (dashed line in Figure 2(e)), reducing the amplitude to 0.13%. On wall B the crests of S and C_θ coincide, raising the amplitude to 11.20%.

Note that C_θ includes the field change due to charge redistribution when the long wall corrugation is added. Its amplitude is nearly the same for both walls, reaching 2.06 (A) and 2.07 (B) times that produced by the isolated long wall corrugation, respectively. Even so, C_θ

alone cannot explain the marked contrast in Figure 1: removing S from the computed inlet field traces increases the maximum relative variation from 4.50% to 10.03% for wall A and decreases it from 14.21% to 8.70% for wall B. The threefold contrast in Figure 1 thus arises from cancellation between S and C_θ on wall A and reinforcement on wall B.

Continuous phase control and parameter robustness—We sweep the spatial phase θ through a full period in steps of 15°. At each phase we solve the steady cold-ion fluid–Poisson system of Eq. (1) on a wall-fitted grid by damped Newton iteration, using preconditioned GMRES for each linear solve. To test the predictive power of Eq. (3), we calibrate the net field increment only at $\theta = 0$ and rotate that single complex coefficient as $C_\theta^{\mathrm{pred}} = C_0 \exp(i\theta)$. This predicts the fundamental amplitude at all remaining 23 phases with no further fitting; adding the same rotating harmonic to the short wall's full inlet trace likewise predicts $\delta_D(H)$ while retaining the shorter-wavelength ripples. As shown in Figure 3(a,b), the predictions closely track the nonlinear sheath solutions: the maximum error in the fundamental amplitude is 0.76% of its peak value, and the maximum error in the full modulation is 0.67 percentage points. Near $\theta = \pi$, the fundamental is nearly extinguished, leaving the shorter harmonics to set the residual inlet modulation.

To verify that this phase sensitivity does not rely on fine-tuned parameters, we repeat the phase sweep under four independent variations: wall bias, inlet Mach number, inlet height, and a detuned short-wave coefficient [Figure 3(c)]. Across all four tests, the ratio of the largest to smallest sampled inlet modulation remains between 2.60 and 3.33. In particular, detuning the mode-12 coefficient from approximately -0.17 to -0.15 restores a finite short-wall vacuum fundamental yet preserves a phase contrast of 3.33. Thus, while the near-null vacuum response cleanly isolates the space-charge mechanism in the benchmark, such tuning is unnecessary for strong phase control.

Implications and a criterion for exterior planar equivalence—Does suppressing the inlet field modulation also suppress the rough wall's signature across the exterior plasma species? For a regular cold-ion sheath near its equipotential inlet, let $e_{\max}(z)$ denote the maximum relative pointwise error over the patch D between the rough-wall solution and the mean-field-matched classical planar sheath across four observables: the potential, the full electric-field vector, and the electron and ion density deficits, normalized, respectively, by $|\bar{\phi}|$, $|\bar{E}_z|$, $n_0 - \bar{n}_e$, and $n_0 - \bar{n}_i$. Near the inlet the potential drop and both density deficits are proportional at leading order to $-E_z(x, H)(H - z)$, with the same factors for the matched plane. The transverse field vanishes at the inlet, so all four normalized errors share the limit

$$\lim_{z \uparrow H} e_{\max}(z) = \delta_D(H). \tag{4}$$

The inlet modulation $\delta_D(H)$ thus provides a criterion for exterior planar equivalence. For a prescribed tolerance ϵ, the matched plane meets the four-field tolerance pointwise on an interval extending to the inlet if $\delta_D(H) < \epsilon$. If $\delta_D(H) > \epsilon$, it exceeds tolerance arbitrarily close to the inlet. This classification is robust to errors in the estimated inlet modulation smaller than the margin $|\delta_D(H) - \epsilon|$. The phase-controlled contrast in $\delta_D(H)$ therefore translates directly into whether the exterior plasma resolves the rough wall or remains equivalent to a single effective plane.

Conclusions—The height PSD alone is insufficient to predict the nonlocal upstream response of a nonlinear plasma sheath. Short-wavelength roughness deflects near-wall ions and excites a long-wavelength space-charge field that survives spatial filtering to the exterior, where it interferes coherently with the response to a macroscopic wall undulation. Sweeping the relative spatial phase continuously tunes the inlet modulation between coherent amplification and shielding at fixed roughness power, and this effect persists robustly across plasma parameters and wall detuning. Comparing the inlet modulation with the prescribed tolerance gives a robust test of exterior planar equivalence. These findings point toward a practical design principle for coherent sheath shielding—positioning fine surface textures relative to macroscopic wall undulations to suppress upstream field variations in plasma processing—and motivate extending rough-wall characterization beyond the PSD to higher-order phase correlations at difference wave numbers.

This work is supported by the Doctoral Scientific Research Start-up Project of Liaoning Provincial Natural Science Foundation (2026-BS-0078, 2026-BS-0402).

[1] M. A. Lieberman and A. J. Lichtenberg, *Principles of Plasma Discharges and Materials Processing* (Wiley, 2005).

[2] Y. Y. Lau, D. Li, and D. P. Chernin, On the Child–Langmuir law in one, two, and three dimensions, Physics of Plasmas **30**, 093104 (2023).

[3] J. W. Brooks and R. Dutta, Sheath thickness measurements with the biased plasma impedance probe: Agreement with Child–Langmuir scaling, Physics of Plasmas **33**, 063502 (2026).

[4] W. Hu, S. Dai, A. Kirschner, and D. Wang, Surface roughness effects on plasma near a divertor plate and local impact angle, Nuclear Materials and Energy **12**, 313 (2017).

[5] G. Memos, E. Lidorikis, and G. Kokkoris, Roughness Evolution and Charging in Plasma-Based Surface Engineering of Polymeric Substrates: The Effects of Ion

Reflection and Secondary Electron Emission, Micromachines **9**, 415 (2018).

[6] National Aeronautics and Space Administration, *Mitigating In-Space Charging Effects—A Guideline*, Tech. Rep. NASA-HDBK-4002B (NASA, 2022).

[7] Y. Li, B. Srinivasan, Y. Zhang, and X.-Z. Tang, Bohm Criterion of Plasma Sheaths away from Asymptotic Limits, Physical Review Letters **128**, 085002 (2022).

[8] I. D. Kaganovich, How to patch active plasma and collisionless sheath: A practical guide, Physics of Plasmas **9**, 4788 (2002).

[9] G. S. Chiu and S. A. Cohen, Comparisons of experimental measurements and two-dimensional plasma-fluid numerical simulations of a magnetized plasma column, Physics of Plasmas **3**, 4250 (1996).

[10] D. Vandembroucq and S. Roux, Conformal mapping on rough boundaries. I. Applications to harmonic problems, Physical Review E **55**, 6171 (1997).

[11] D. Kim, D. J. Economou, J. R. Woodworth, P. A. Miller, R. J. Shul, B. P. Aragon, T. W. Hamilton, and C. G. Willison, Plasma molding over surface topography: simulation and measurement of ion fluxes, energies and angular distributions over trenches in RF high density plasmas, IEEE Transactions on Plasma Science **31**, 691 (2003).

[12] V. P. BUDAEV and M. YAKOVLEV, On Fractal Properties of Equipotentials over a Real Rough Surface Faced to Plasma in Fusion Devices, Plasma and Fusion Research **3**, 001 (2008).

[13] F. Detering, A. Smolyakov, and I. Khabibrakhmanov, Transverse stability of strongly nonlinear ion acoustic modes, Physics Letters A **324**, 465 (2004).

[14] X.-Z. Tang and Z. Guo, Kinetic model for the collisionless sheath of a collisional plasma, Physics of Plasmas **23**, 083503 (2016).

[15] E. Stamate and H. Sugai, Modal Focusing Effect of Positive and Negative Ions by a Three-Dimensional Plasma-Sheath Lens, Physical Review Letters **94**, 125004 (2005).